

Supplementary Online Materials for

Coupled motion of Xe clusters and quantum vortices in He nanodroplets

Authors: Curtis F. Jones, Charles Bernando, Rico Tanyag, Ken R. Ferguson, Camila Bacellar, Luis Gomez, Denis Anielski, Ali Belkacem, Rebecca Boll, John Bozek, Sebastian Carron, James Cryan, Lars Englert, Sascha W. Epp, Benjamin Erk, Robert Hartmann, Lutz Foucar, Daniel M. Neumark, Daniel Rolles, Benedikt Rudek, Artem Rudenko, Katrin R. Siefermann, Felix P. Sturm, Joachim Ullrich, Fabian Weise, Christoph Bostedt, Oliver Gessner, Andrey F. Vilesov

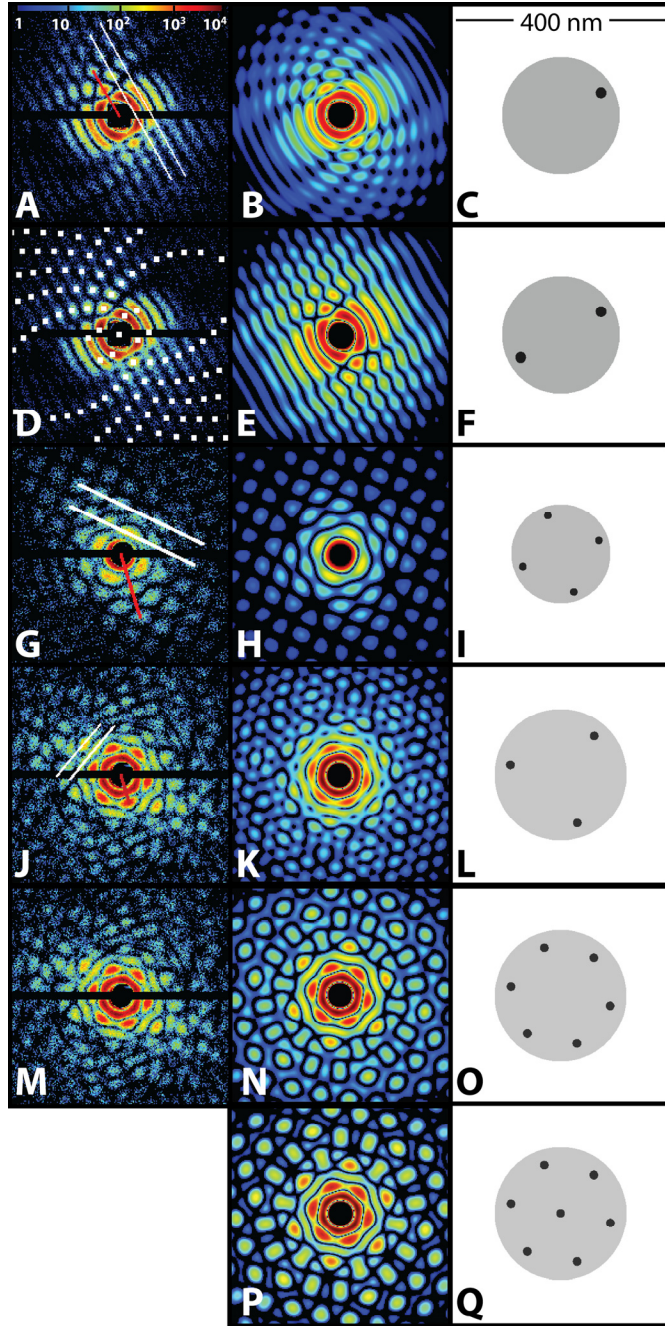


FIG. S1. Analytical modeling of measured diffraction patterns. The experimental images in the left column are modeled by analytically derived diffraction patterns as shown in the center column. The right column shows the spatial arrangements of Xe clusters (black) inside He droplets (gray) that give rise to the simulated diffraction patterns. The data displayed in A and D are identical and correspond to Fig. 2B1 of the main article, except here they are plotted against a black background. Similarly, panel G corresponds to Fig. 2C1 and panels J, M to Fig. 2D1 of the main article.

S1: Calculation of Cluster Coordinates from Symmetric Diffraction Images

Although the cluster configurations presented in the main text were ultimately obtained by the application of an iterative phase retrieval algorithm [1], the highly symmetric diffraction patterns also invite an analytic estimate of the cluster arrangements. A comparison of the results of these independent approaches validates the results presented in the main text. We model the recorded images by comparison with X-ray diffraction arising from a droplet of radius R_D containing a small number, N , of spherical Xe clusters, each having the same radius $R_C \ll R_D$. The total scattering amplitude of these systems is given by the coherent superposition of the scattering amplitudes S_D and S_C from the droplet and the embedded identical clusters, respectively; the intensity recorded at the detector is given by

$$I = \left| S_D(q, R_D) + S_C(q, R_C) \cdot \sum_{j=1}^N e^{-i(\vec{q} \cdot \vec{d}_j)} \right|^2. \quad (1)$$

Herein, $q = |\vec{q}|$ is the change in the incident wavevector upon scattering and \vec{d}_j represents the position of the j^{th} cluster with respect to the droplet center. For the current case of small-angle scattering ($\Theta < 0.02$ rad) $\vec{q} \cdot \vec{d}_j \approx q_x x_j + q_y y_j$, in which x_j and y_j are cluster coordinates in the plane perpendicular to the X-ray beam.

The amplitude of a diffracted plane wave due to a spherical object of radius R is given by [2]

$$S(q, R) \propto \frac{(1-n) \cdot R}{q^2} \cdot \left[\frac{\sin(q \cdot R)}{q \cdot R} - \cos(q \cdot R) \right], \quad (2)$$

in which n is the complex refractive index of the scattering medium, e.g. He or Xe. We assume, for simplicity, that the ratio of the $(1-n)$ values for Xe and He is real and given by

$\sqrt{|1-n_{Xe}|^2} / \sqrt{|1-n_{He}|^2} = 19.9$. This estimate is based on atomic scattering factors and the assumption that clusters and droplets have densities of solid Xe and liquid He, respectively [3]. Although we consider spherical clusters here, we note that Xe clusters formed inside

vortices may have irregular or even filament-like shapes (Figs. 2E2 and 2F2 of the main text).

We first discuss a He droplet containing a single Xe cluster ($N = 1$), displaced by a distance, d , relative to the droplet center along the Y-axis. In this case, the diffraction intensity is given by

$$\begin{aligned} I &= \left| S_D(q, R_D) + S_C(q, R_C) \cdot e^{-i(q_y d)} \right|^2 \\ &= S_D(q, R_D)^2 + S_C(q, R_C)^2 + 2 \cdot S_D(q, R_D) \cdot S_C(q, R_C) \cdot \cos(q_y d) \end{aligned} \quad (3)$$

The zero-order diffraction maximum of the small Xe cluster will occupy most, if not all, of the detector, and can be approximated by a positive constant due to the order-of-magnitude size difference between the Xe clusters and the He droplets. Outside the central detector hole, the signal intensity variations due to the droplet are well approximated by a negative cosine function. Therefore, eq. (3) can be approximated by

$$I \approx A_D^2 \cdot \frac{\cos^2(q R_D)}{q^4} + A_C^2 - \frac{2 \cdot A_D \cdot A_C \cdot \cos(q R_D) \cdot \cos(q_y d)}{q^2}, \quad (4)$$

wherein A_D and A_C are the He droplet and Xe cluster amplitude factors, respectively. The third term in eq. (4) represents the interference between the droplet and cluster diffraction patterns. Interference maxima occur either when $q_y d = 2m\pi$; $m = \dots, -1, 0, 1, \dots$ and $q R_D = (2k+1)\pi$; $k = 0, 1, 2, \dots$, or when $q_y d = (2m+1)\pi$; $m = \dots, -1, 0, 1, \dots$ and $q R_D = 2k\pi$; $k = 0, 1, 2, \dots$. Geometrically, this occurs when the linear fringes that align perpendicular to the cluster displacement axis (i.e. along the X-axis) intersect in phase with the rings from the droplet. The coordinates of the interference maxima, D_X , D_Y , in detector space are

$$D_Y = \frac{\lambda Z}{2} \cdot \frac{m}{d} \quad ; \quad D_X = \frac{\lambda Z}{2} \sqrt{\frac{k^2}{R_D^2} + \frac{m^2}{d^2}} \quad ; \quad k = [0, 1, 2, \dots] \quad ; \quad m = [\dots, -1, 0, 1, \dots], \quad (5)$$

in which Z is the distance between the scattering center and the detector and the indices k and m enumerate the droplet rings and interference fringes, respectively.

We used eqs. (1-5) to simulate the experimental diffraction intensities shown in the left column of Fig. S1 using the model cluster arrangements shown in the right column. The simulated diffraction pattern shown in Fig. S1B, for example, emerges from a single cluster in the droplet, depicted in Fig. S1C. The positions of the diffraction maxima from two symmetrically displaced clusters in a He droplet (Fig. S1F) are also described by eq. (5), the corresponding pattern is depicted in Fig. S1E. It resembles the experimental data much more closely than the simulation in Fig. S1B. The single cluster pattern in Fig. S1B has much less contrast and fails to reproduce the linear fringes. Therefore, we ascribe the diffraction in Fig. 2B1 of the main text to a droplet containing two clusters that are symmetrically separated from the droplet center as depicted in Fig. S1F. Values of the droplet radius ($R_D = 107$ nm) and the cluster displacement ($d = 81$ nm) were calculated by measuring D_X and D_Y in Fig. S1A. The spacing between the linear fringes was measured between the parallel white lines, while the spacing between the rings was measured along the single red line emanating from the center. The positions of the maxima obtained from inserting these values into eq. (5) are shown in Fig. S1D as white dots, demonstrating excellent agreement with the experimental data.

A similar treatment has been applied to the data in Fig. S1G and Figs. S1J,M, which are identical to Fig. 2C1 and Fig. 2D1, respectively, in the main text, except on a black background. The modeling becomes more ambiguous as the system complexity grows due to the larger number of scattering centers. For this reason, the clusters were assumed to be identical in size and symmetrically distributed about the droplet center, which is justified by the high degree of symmetry of the observed patterns. The fourfold symmetry present in panel S1G suggests a square-symmetric cluster arrangement. The simplest example of this is

a constellation of four clusters arranged in a square centered in the droplet. This arrangement will produce linear interference fringes for each pair of oppositely placed clusters, intersecting at 90° angles. The separation between the fringes gives $d = 73$ nm, while the separation between the droplet circular fringes gives $R_D = 90$ nm. The simulated pattern in Fig. S1H reproduces the data in Fig. S1G very well.

At first glance, the six-fold symmetry of Fig. S1J suggests a triangular cluster arrangement, which is supported by the presence of linear fringes that intersect at 60° . $R_D = 120$ nm is straightforwardly determined from the droplet's circular fringes, while the linear fringe separation indicates a cluster displacement of $d = 93$ nm. However, the simulated diffraction in Fig. S1K, derived from the three clusters depicted in Fig. S1L, lacks correspondence with Fig. S1J just as Fig. S1B fails to reproduce the data in Fig. S1A. Note that two superimposed triangles rotated 60° with respect to one another form a regular hexagon, which also produces linear diffraction fringes that intersect at 60° . Figure S1N shows the simulated diffraction pattern produced by the hexagonal arrangement in Fig. S1O, which reproduces the central regions of the experimental image much more closely than Fig. S1K. Figure S1P shows the simulated diffraction pattern produced by a hexagonal arrangement with a central cluster as depicted in Fig. S1Q. Similarly to the triangular cluster arrangement, this cluster configuration leads to noticeable deviations in the diffraction pattern at large q compared to the six-membered ring in Fig. S1O. However, the deviations between the different models occur in the intensity distribution, whereas the symmetry of the diffraction patterns remains the same. Strong support for a cluster configuration similar to the one illustrated in Fig. S1O is also provided by the DCDI density reconstruction discussed here and in the main text.

The droplet radii and average distances of the clusters from the droplet center obtained from the modeling are listed in Table S1. Table S2 shows the Xe atom partitioning

between the clusters and the radial displacements and azimuthal angles of the clusters taken from the density reconstructions in Figs. 2B2-D2 of the main text. The phase retrieval results provide more detailed information on the cluster arrangement, and they are also in good agreement with the analytical modeling, providing independent support for the density calculations.

We have also tested the effect of the presence of a central cluster in the hexagonal configuration on the quality of the reconstruction, as determined by the normalized root mean square deviation (NRMSD) of the calculated and measured diffraction patterns [1]. The NRMSD between the diffraction patterns in Fig.1D1 and D3 of the main article was found to be 0.3952, which is mainly determined by the shot noise in the experimental diffraction. For comparison, we have artificially magnified the central feature in Fig.1D2 so that the total Xe density remains the same and the central feature contains 1/7 of the total density. The resulting diffraction pattern leads to an NRMSD value of 0.4313, which is larger than that in the original reconstruction. This deviation is statistically significant because the shot noise uncertainty of the NRMSD determination is $2\sigma = 0.0015$. On the other hand, removing the central feature altogether gives the NRMSD = 0.3970. Thus the change of the NRMSD between the structures with and without the central feature is comparable to the NRMSD uncertainty due to shot noise and is not statistically significant.

TABLE S1. Droplet radius (R_D), average distance (d) of the clusters from the droplet center, and average radius (R_C) of the clusters obtained from modeling the data in Figs. S1D, G, M by diffraction patterns from symmetric arrangements of identical spheres.

Number of clusters	2	4	6
R_D [nm]	107	90	120
d [nm]	81	73	93
R_C [nm]	10	7	8

TABLE S2. Xe atom partitioning between the clusters, radial displacements, and azimuthal angles ϕ of the cluster positions as obtained from the iterative phase retrieval density reconstructions. The angle is counted counterclockwise from the horizontal axis in Figs. 2B2, C2, and D2 of the main text. Uncertainties are root mean square deviations of the measured values and the averages.

		Fraction of N_{Xe} in a cluster	Distance from the center of the droplet, nm	ϕ , degrees	$\Delta\phi$, degrees
Fig. 2B2			$R_D = 108 \pm 6$ nm		
	1	0.50	82 ± 12	33 ± 7	187
	2	0.50	83 ± 11	206 ± 8	173
	Ave	0.50	83 ± 8		180 ± 8
Fig. 2C2			$R_D = 90 \pm 5$ nm		
	1	0.26	73 ± 10	18 ± 6	87
	2	0.23	72 ± 10	108 ± 5	90
	3	0.25	68 ± 13	198 ± 5	90
	4	0.26	72 ± 10	291 ± 7	93
	Ave	0.25 ± 0.02	71 ± 5		90 ± 4
Fig. 2D2			$R_D = 118 \pm 6$ nm		
	1	0.18	91 ± 15	16 ± 7	57
	2	0.15	87 ± 15	77 ± 9	61
	3	0.16	98 ± 11	140 ± 8	63
	4	0.19	92 ± 15	198 ± 7	58
	5	0.14	90 ± 8	255 ± 7	57
	6	0.19	97 ± 13	319 ± 9	64
	Ave	0.17 ± 0.02	92 ± 5		60 ± 5

S2. Calculation of N_{Xe} from the Pickup Pressure and Observed Droplet Radius.

The average initial droplet size and the average number of captured Xe atoms are determined at the beginning of each experimental run using a titration technique developed by Gomez et al [4]. However, the actual size of individually imaged droplets may deviate considerably from the average value due to the broad droplet size distribution in the beam [5]. For each specific imaged droplet, the number of captured Xe atoms is obtained from the radius of the doped droplet as determined from the diffraction image and the absolute Xe pickup pressure. Eq. (6) gives the instantaneous frequency of successive collisions for a droplet of radius R_D traveling at a speed v_D through Xe gas with a thermal velocity v_{Xe} and number density η_{Xe} :

$$f_C = \eta_{\text{Xe}} \cdot \pi R_D^2 \sqrt{v_D^2 + v_{\text{Xe}}^2} \quad (6)$$

This equation is used to calculate the number of collisions the droplet experiences while traversing the pick-up cell, taking into account the reduction in droplet size upon collision-induced evaporative cooling. We assume the droplet evaporates 250 helium atoms per Xe collision, based on the thermal and cohesive energies of Xe atoms and the evaporation enthalpy of He. Thus, starting at the final droplet size and propagating the droplet backward in time through the pickup cell, we account for the instantaneous change in the droplet cross-section and simulate the droplet evaporation in reverse to provide the number of captured Xe atoms, given in Table 1 of the main text.

S3. Radial position of a doped vortex in a freely rotating cylindrical droplet.

In order to gain insight into the effect of doping on the vortex coordinates, we have studied the model of a freely rotating superfluid cylinder with constant total angular momentum, L . The model is similar to that previously discussed in Ref. [6], however instead

of the rotation of the normal component, we have assumed that the droplet is entirely superfluid and the classical angular momentum is associated only with the Xe atoms embedded in the vortex core. The stable configuration of a vortex at distance r from the center corresponds to a minimum energy, E , in the laboratory frame. Neglecting any backflow effects, the energy and angular momentum per unit length are [7]:

$$E = \frac{\rho_{He} \kappa^2}{4\pi} \ln\left(\frac{R_{He}^2 - r^2}{R_{He}^2 \xi}\right) + \frac{\rho_{Xe} \cdot \pi \cdot R_{Xe}^2 \cdot (0.5 \cdot R_{Xe}^2 + r^2) \cdot \omega^2}{2} + V(r)$$

$$L = \frac{\rho_{He} \kappa}{2} (R_{He}^2 - r^2 - R_{Xe}^2) + \rho_{Xe} \cdot \pi \cdot R_{Xe}^2 \cdot (0.5 \cdot R_{Xe}^2 + r^2) \cdot \omega$$

where $\rho_{He} = 145 \text{ kg/m}^3$ and $\rho_{Xe} = 3781 \text{ kg/m}^3$ are the densities of liquid helium and of solid Xe, respectively, $\kappa = 9.97 \times 10^{-8} \text{ m}^2/\text{s}$ is the quantum of circulation, ω is the angular velocity of the vortex, R_{He} is the radius of the cylinder and R_{Xe} is the radius of the embedded Xe filament. In the absence of Xe the radius of a vortex is $\xi = 10^{-10} \text{ m}$, whereas with Xe it is approximated by R_{Xe} . $V(r)$ is the solvation potential, which was calculated from the Lennard-Jones pair potential of the interaction between He and Xe atoms. $V(r)$ is set to zero in the cylinder's center and increases sharply about 10 nm from the surface.

The cross markers in Fig. S2 show the results of the calculations of r vs L for $R_{He} = 100 \text{ nm}$ and $R_{Xe} = 5 \text{ nm}$. For comparison, the corresponding results for a bare vortex line are shown by a continuous curve. It is seen that the presence of a Xe filament generally leads to an increase of r that can be ascribed to a centrifugal force on the vortex. In addition, doped vortices cannot come too close to the surface due to the solvation potential, leading to a maximum radial position of $r_{\max} \approx 90 \text{ nm}$. In principle, similar equations should govern the behavior of multiple vortices in a droplet. However, this more complex situation cannot be

treated in an as straightforward fashion as outlined above since the shape of multiply doped (and bare) vortices in a spheroidal droplet requires state of the art calculations,[8] which are beyond the scope of the present paper.

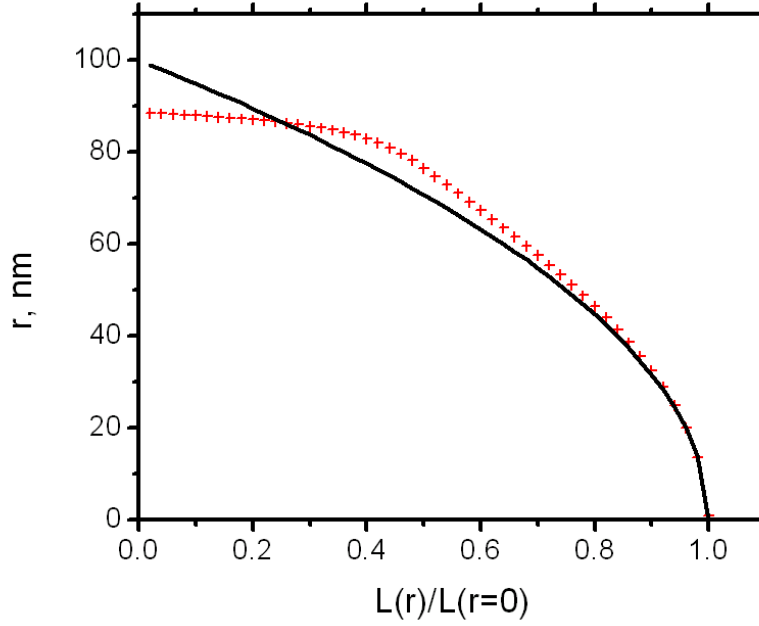


Figure S2. Calculated equilibrium distance r of a vortex from the center of an $R_{He} = 100$ nm cylinder filled with superfluid helium. The distance r is plotted versus the total angular momentum of the system, which is given in units of the angular momentum of a central bare vortex. The continuous curve and cross markers represent the results for a bare vortex and for a vortex containing a filament of solid Xe with $R_{Xe} = 5$ nm, respectively.

References

1. R.M. Tanyag, C. Bernando, C.F. Jones, C. Bacellar, K. Ferguson, D. Anielski, R. Boll, S. Carron, J. Cryan, L. Englert, S. Epp, B. Erk, L. Foucar, L. Gomes, R. Hartmann, D. Neumark, D. Rolles, B. Rudek, K. Siefermann, J. Ullrich, F. Weise, C. Bostedt, O. Gessner, and A.F. Vilesov, *X-ray coherent diffraction imaging by immersion in nanodroplets*. Structural Dynamics, **2**: 051102-1-9 (2015).
2. M. Kerker, *The scattering of light and other electromagnetic radiation*. 1969, New York: Academic Press.
3. B.L. Henke, E.M. Gullikson, and J.C. Davis, *X-ray interactions - photoabsorption, scattering, transmission, and reflection at $E=50\text{-}30,000\text{ eV}$, $Z=1\text{-}92$* . Atom. Data .Nucl. Data Tables, **54**: 181-342 (1993).
4. L.F. Gomez, E. Loginov, R. Sliter, and A.F. Vilesov, *Sizes of large helium droplets*. J. Chem. Phys., **135**: 154201-1-9 (2011).
5. R. Sliter, L. Gomez, J. Kwok, and A.F. Vilesov, *Size Distributions of Large He Droplets*. Chem. Phys. Lett., **600**: 29-33 (2014).
6. G.H. Bauer, R.J. Donnelly, and W.F. Vinen, *Vortex Configurations in a Freely Rotating Superfluid Drop*. J. Low Temp. Phys., **98**: 47-65 (1995).
7. G.B. Hess, *Angular Momentum of Superfluid Helium in a Rotating Cylinder*. Phys. Rev., **161**: 189-193 (1967).
8. F. Ancilotto, M. Pi, and M. Barranco, *Vortex arrays in nanoscopic superfluid helium droplets*. Phys. Rev. B, **91**: 100503(R)-1-5 (2015).